Geophysical Journal International

Geophys. J. Int. (2016) **206,** 1315–1326
Advance Access publication 2016 June 15
GJI Seismology

doi: 10.1093/gji/ggw212

Accuracy of the water column approximation in numerically simulating propagation of teleseismic *PP* waves and Rayleigh waves

Yong Zhou,[1,2] Sidao Ni,[1] Risheng Chu[1] and Huajian Yao[3]

[1] *State Key Laboratory of Geodesy and Earth's Dynamics, Institute of Geodesy and Geophysics, Wuhan* 400077*, China. E-mail: sdni@whigg.ac.cn*
[2] *University of Chinese Academy of Sciences, Beijing* 100049*, China*
[3] *Mengcheng National Geophysical Observatory, University of Science and Technology of China, Hefei* 230026*, China*

Accepted 2016 June 1. Received 2016 June 1; in original form 2016 February 6

SUMMARY

Numerical solvers of wave equations have been widely used to simulate global seismic waves including *PP* waves for modelling 410/660 km discontinuity and Rayleigh waves for imaging crustal structure. In order to avoid extra computation cost due to ocean water effects, these numerical solvers usually adopt water column approximation, whose accuracy depends on frequency and needs to be investigated quantitatively. In this paper, we describe a unified representation of accurate and approximate forms of the equivalent water column boundary condition as well as the free boundary condition. Then we derive an analytical form of the *PP*-wave reflection coefficient with the unified boundary condition, and quantify the effects of water column approximation on amplitude and phase shift of the *PP* waves. We also study the effects of water column approximation on phase velocity dispersion of the fundamental mode Rayleigh wave with a propagation matrix method. We find that with the water column approximation: (1) The error of *PP* amplitude and phase shift is less than 5 per cent and 9° at periods greater than 25 s for most oceanic regions. But at periods of 15 s or less, *PP* is inaccurate up to 10 per cent in amplitude and a few seconds in time shift for deep oceans. (2) The error in Rayleigh wave phase velocity is less than 1 per cent at periods greater than 30 s in most oceanic regions, but the error is up to 2 per cent for deep oceans at periods of 20 s or less. This study confirms that the water column approximation is only accurate at long periods and it needs to be improved at shorter periods.

Key words: Numerical approximations and analysis; Body waves; Surface waves and free oscillations; Theoretical seismology; Wave propagation.

1 INTRODUCTION

Thanks to the ever increasing computational power, numerical simulation of global seismic wave propagation has become an effective approach for studying structure and dynamics of the Earth, with methods such as finite difference method, finite element method, pseudospectral method and spectral element method (SEM; Igel *et al.* 1995; Bao *et al.* 1998; Cormier 2000; Wang *et al.* 2001; Komatitsch *et al.* 2002; Capdeville *et al.* 2005; Zhang & Chen 2006; Moczo *et al.* 2007). The finite difference method can be implemented straightforwardly for serial or parallel computation with high efficiency (Igel *et al.* 1995; Zhang & Chen 2006). The finite element method can deal with complex topography and unstructured meshes, thus is particularly desirable for geologically complex regions (Bao *et al.* 1998; Moczo *et al.* 2007). The pseudospectral method accurately calculates spatial derivatives in the wave number domain with a fast Fourier transform, therefore boasting of high speed and low numerical dispersion (Cormier 2000; Wang *et al.* 2001). The SEM combines the flexibility of the finite-element method and the accuracy of the pseudospectral method, and can handle simulation of complicated Earth models, including topography, lateral heterogeneity, sharp contrasts and self-gravitation (Komatitsch *et al.* 2002; Komatitsch & Tromp 2002a,b). In conjunction with abundant waveform data from global seismic networks, the above numerical methods have been widely applied to study structures of the Earth's interior (Igel *et al.* 1995; Cormier 2000; Zhang & Chen 2006; Baker & Roecker 2014) and earthquake source parameters (Liu *et al.* 2004).

These methods treat the land surface as a free boundary with zero traction. While in the oceanic area which covers most of the Earth's surface, the surface is assumed to be a free boundary with zero pressure, and the seafloor has a boundary condition of continuity of normal component of traction and particle displacement or velocity (i.e. zero tangential traction, and no tangential displacement or velocity involved). However, acoustic wave speed in the ocean is usually significantly smaller than *P* or *S* wave speed in the crust, therefore, finer mesh is needed in the numerical simulation of seismic wave propagation, which results in a significant increase in memory requirement and computing time. Moreover, it is difficult and ineffective in terms of numerical cost to mesh the

continent-ocean margin if the ocean water is meshed (Capdeville & Marigo 2008). Similar problem occurs in the studies of electromagnetic scattering and acoustics, some researchers find that the effective boundary method can be used to dramatically reduce the computation cost without much loss of accuracy (Niklasson *et al.* 2000; Zakharov 2006; Péron 2014). As the first order term of the above effective boundary for wave propagation in the fluid layer, Komatitsch & Tromp (2002b) assume that the entire water column moves at the same particle velocity, and derive the effective boundary equation of ocean water column loading in the SEM scheme (eq. 28 in Komatitsch & Tromp 2002b). In this case, the pressure load is a product of density, thickness of ocean water and normal component of the particle acceleration of the seafloor. After adopting this water column approximation (WCA), there is no need to simulate seismic wave propagation in the ocean water, and effects of the ocean water are accounted for with a new boundary condition on the surface of the solid Earth instead of a free boundary condition, thus the computational efficiency is improved effectively. Therefore, SEM with this approximation has been widely used in global seismic wave simulation because of improved performance and convenience in constructing meshes. For example, SEM is successfully adopted in regional and global tomographic inversions, which reveal interior of the Earth with unprecedented details (Tape *et al.* 2009; Chen *et al.* 2015; French & Romanowicz 2015).

SEM also plays an important role on studies of *PP* waves (Ritsema *et al.* 2002) and Rayleigh waves (Stich & Morelli 2007; Bozdağ & Trampert 2008; Ruan & Zhou 2012; Liu & Zhou 2013). The unique geometry of *PP* ray paths makes it sensitive to structures underneath the midpoints between the earthquake and seismic station. Compared with the direct *P* waves, mantle structures under the oceans are much better sampled with *PP* waves and *PP* precursors due to reflection at mantle discontinuities such as the 410 and 660 discontinuities (Fukao *et al.* 2003). The differential times between *PP* waves and *PP* precursors as well as their amplitude ratios provide crucial information of depth and velocity contrast of the mantle discontinuities (Deuss *et al.* 2006; Deuss 2009). In these studies, *PP* waves are assumed to be normal and thus can be used as an effective reference phase. However, as shown by Ritsema *et al.* (2002), *PP* amplitude shows variability due to 3-D structures. Furthermore, as will be demonstrated later on, the *PP* reflection coefficient is not a real number but complex for the effective boundary condition of WCA, thus leading to a phase shift (equivalent to time shift) and change of reflection amplitude. Therefore, it is necessary to quantify the effects of WCA on *PP* waves when SEM is used to simulate global *PP* waves. Furthermore, Rayleigh waves usually dominate teleseismic waveforms, and provide valuable information for study of crustal and upmost mantle structure of the Earth and have been used extensively in global or regional tomography (Yao *et al.* 2006; Yang *et al.* 2007; Yao *et al.* 2008; Ekström 2011). As the majority of the Earth's surface is covered with ocean water, the effects of WCA on surface wave dispersion also need to be explored in order to achieve robust tomography of crustal and mantle structure.

Indeed, the accuracy of the approximation in simulating body and surface waves has been qualitatively investigated, either by comparing with exact solution or with observed seismic data. Komatitsch & Tromp (2002b) reported that WCA is only valid at periods greater than 20 s when the thickness of ocean is 3 km, as they observed that the synthetic seismograms computed by SEM with WCA match well with normal-modes calculations at periods greater than 25 s. Komatitsch *et al.* (2002) also found that the observed seismic waves are usually well explained with synthetics for body waves with periods greater than 18 s and surface waves with periods greater than 40 s. But at shorter periods, there could be substantial mismatch, and they suspected that it may result from inaccurate crust model or the WCA. Theoretically, the effectiveness of WCA relies on the ratio between the thickness of ocean water and seismic wave length, and higher accuracy should be expected for small ratios. However, the thickness of ocean water ranges from dozens of meters in coastal regions to more than 10 km in the deepest subduction trench. It is expected that for some oceanic region, the error of WCA may be substantial when the ocean bathymetry is comparable to seismic wave length.

Therefore, we investigate quantitatively the accuracy of WCA in this paper. We first derive a unified boundary condition that can account for free surface, the precise and approximate forms of water column loading effects. Then, we derive an analytical form of *PP* reflection coefficient, and explore the effects of WCA on the amplitude and phase shift of *PP* reflection. We also explore the effects of WCA on surface wave dispersion, after we implement an algorithm in computing phase velocity of fundamental mode Rayleigh waves for multilayered half-space models (Chen 1993). In the last, we discuss limitation of our approach and further studies that could be performed in the future.

2 A UNIFIED SURFACE BOUNDARY CONDITION WITH A FLUID LAYER

In contrast to the free surface boundary condition, the normal component of the traction (T_n) on seafloor is no longer zero, though the tangential component can be reasonably assumed to be zero ($T_t = 0$). The approach of effective boundary condition such as WCA attempts to relate the normal traction T_n with particle acceleration, thus introducing mixed boundary condition. For the case of incident planar wave on a water layer of constant thickness H, exact boundary condition can be obtained by applying the condition of zero tangential traction, and continuity of normal traction and particle displacement (Figs 1a and b). For simplicity, the solid Earth is parameterized as a homogeneous half-space.

As there is only longitudinal wave in seawater, the wavefield in the water layer can be decomposed into upgoing and downgoing *P* waves. Within the framework of planar wave theory (Aki & Richards 2002), the *P*-wave potential in the water layer is as follows (sign convention is positive for downwards in the Z direction):

$$\phi_w = C_u \exp[i\omega(px - \eta_w z - t)] + C_d \exp[i\omega(px + \eta_w z - t)] \tag{1}$$

with

$$\eta_w = \sqrt{\frac{1}{{\alpha_w}^2} - p^2} = \sqrt{\frac{1}{{\alpha_w}^2} - \frac{1}{c^2}},$$

where C_u and C_d are the coefficients for upgoing and downgoing *P* wave, respectively, and p is the horizontal slowness, α_w is *P*-wave velocity in fluid layer, η_w is also called the vertical slowness and $c = 1/p$ is the phase velocity.

Since the bulk modulus of air is orders of magnitude smaller than that of the water, the surface of the ocean is considered a free boundary on which the traction is zero. Based on eq. 5.21 in Aki & Richards (2002), and imposing the free boundary condition into eq. (1), we get

$$C_u \exp(i\omega\eta_w H) + C_d \exp(-i\omega\eta_w H) = 0. \tag{2}$$

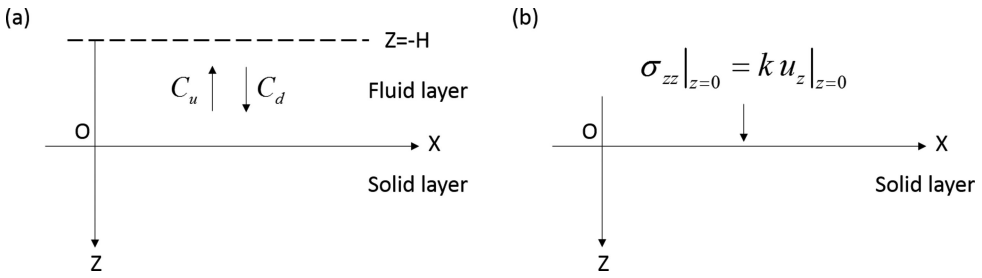

Figure 1. Geometry and coordination system of water column approximation. (a) Upgoing and downgoing *P* (acoustic) wave in a homogeneous fluid layer with thickness *H* over a half-space solid Earth. (b) The acoustic wave propagation is approximated with effective boundary condition involving of normal traction and vertical displacement on the boundary.

Then a new coefficient C can be defined to relate C_u and C_d:

$$C_u = \frac{C}{2}\exp(-i\omega\eta_w H)$$
$$C_d = -\frac{C}{2}\exp(i\omega\eta_w H). \tag{3}$$

The wavefield in the fluid layer can be rewritten as

$$\phi_w = \frac{C}{2}\exp(-i\omega\eta_w H)\exp[i\omega(px-\eta_w z-t)] - \frac{C}{2}\exp(i\omega\eta_w H)\exp[i\omega(px+\eta_w z-t)] \tag{4}$$

Also based on eq. 5.21 in Aki & Richards (2002) and eq. (4), the normal component of particle displacement in the sea layer is

$$u_z = -\frac{1}{2}i\omega\eta_w C\exp[i\omega(px-t)] \times\left[\exp(i\omega\eta_w H)\exp(i\omega\eta_w z) + \exp(-i\omega\eta_w H)\exp(-i\omega\eta_w z)\right] \tag{5}$$

and the normal stress is

$$\sigma_{zz} = \frac{1}{2}\rho_w\omega^2 C\exp[i\omega(px-t)] \times\left[\exp(i\omega\eta_w H)\exp(i\omega\eta_w z) - \exp(-i\omega\eta_w H)\exp(-i\omega\eta_w z)\right]. \tag{6}$$

Therefore, the normal component of particle displacement on the seafloor is

$$u_z|_{z=0} = -i\omega\eta_w\cos(\omega\eta_w H)C\exp[i\omega(px-t)] \tag{7}$$

and the normal traction is

$$T_n = \sigma_{zz}|_{z=0} = i\rho_w\omega^2\sin(\omega\eta_w H)C\exp[i\omega(px-t)] \tag{8}$$

Combining eqs (7) and (8), we get the following relationship:

$$\sigma_{zz}|_{z=0} = -\frac{\rho_w\omega}{\eta_w}\tan(\omega\eta_w H)u_z|_{z=0}. \tag{9}$$

When $\omega\eta_w H$is sufficiently small, eq. (9) can be approximated as

$$\sigma_{zz}|_{z=0} = -\rho_w\omega^2 H u_z|_{z=0}, \tag{10}$$

which is consistent with equations (eqs 26–28) of WCA in Komatitsch & Tromp (2002b).

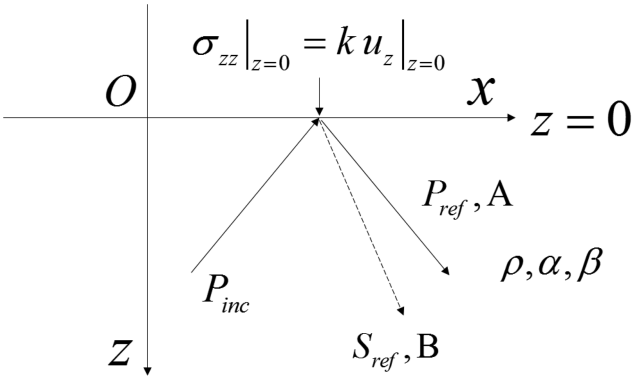

Figure 2. Incident *P* wave and reflect *P* wave and *SV* wave with the unified boundary condition. The density, *P*-wave velocity and *S*-wave velocity are denoted as ρ, α and β, respectively. The incident *P* wave is normalized (coefficient is 1). A and B are the coefficients of the reflected *P* and *S* waves.

For the case that the thickness of fluid layer is zero, eq. (9) is just reduced to free boundary condition:

$$\sigma_{zz}|_{z=0} = 0. \tag{11}$$

Actually, eqs (9)–(11) can be represented with a unified form

$$\sigma_{zz}|_{z=0} = k u_z|_{z=0}, \tag{12}$$

where, for the exact boundary condition of a fluid layer,

$$k = -\frac{\rho_w\omega}{\eta_w}\tan(\omega\eta_w H) \tag{13}$$

for the approximate boundary condition,

$$k = -\rho_w\omega^2 H \tag{14}$$

and for the case of free boundary condition, k is just 0.

3 THE EFFECTS ON *PP* WAVES OF WCA

To investigate the effects of WCA on *PP* wave propagation, we compute the amplitude and phase of *PP* waves reflected at seafloor. As shown in Fig. 2, a plane *P* wave is propagating with slowness p, then *P* wave and *SV* wave are generated after reflection. The thickness of fluid layer is H, the density and *P*-wave velocity of water are ρ_w and α_w, respectively. The density, *P*-wave velocity and *S*-wave velocity in the solid half-space are ρ, α and β, respectively. The coefficient of incident *P*-wave potential is normalized as 1, and the coefficients of reflect *P*- and *S*-wave potentials are denoted as A and B, respectively.

Based on the assumption of plane wave, the incident *P*-wave, reflected *P*-wave and *S*-wave potential functions are as follows:

$$\phi_{\text{inc}} = \exp[i\omega(px - \eta_\alpha z - t)] \tag{15}$$

$$\phi_{\text{ref}} = A\exp[i\omega(px + \eta_\alpha z - t)] \tag{16}$$

$$\psi_{\text{ref}} = B\exp[i\omega(px + \eta_\beta z - t)], \tag{17}$$

where

$$\eta_\alpha = \sqrt{\frac{1}{\alpha^2} - p^2} = \sqrt{\frac{1}{\alpha^2} - \frac{1}{c^2}} \tag{18}$$

$$\eta_\beta = \sqrt{\frac{1}{\beta^2} - p^2} = \sqrt{\frac{1}{\beta^2} - \frac{1}{c^2}}. \tag{19}$$

For the solid–fluid interface (the seafloor), the shear traction is zero. Based on eqs 5.21 and 5.22 in Aki & Richards (2002) and eqs (15)–(17) above, we get

$$2\rho\beta^2 i\omega p i\omega\eta_\alpha (A-1) + \rho\omega^2\left(1 - 2\beta^2 p^2\right) B = 0. \tag{20}$$

Similarly, the normal displacement and normal traction from the side of solid half-space are

$$u_z|_{z=0} = [i\omega\eta_\alpha (A-1) + i\omega pB]\exp[i\omega(px - t)] \tag{21}$$

$$\sigma_{zz}|_{z=0} = \left[-\rho\omega^2(1-2\beta^2p^2)(A+1) + 2\rho\beta^2 i\omega p i\omega\eta_\beta B\right] \times \exp[i\omega(px - t)]. \tag{22}$$

Eqs (21) and (22) are related as follows:

$$\left.\frac{\sigma_{zz}}{u_z}\right|_{z=0} = \frac{-\rho\omega^2(1-2\beta^2p^2)(A+1) + 2\rho\beta^2 i\omega p i\omega\eta_\beta B}{i\omega\eta_\alpha (A-1) + i\omega pB}. \tag{23}$$

Solving eqs (20) and (23) and imposing the unified boundary condition (eq. 12), we find that

$$A = \frac{-\left(1-2\beta^2p^2\right)^2 + 4\beta^4p^2\eta_\alpha\eta_\beta + i\frac{\eta_\alpha}{\rho\omega}k}{\left(1-2\beta^2p^2\right)^2 + 4\beta^4p^2\eta_\alpha\eta_\beta + i\frac{\eta_\alpha}{\rho\omega}k} \tag{24}$$

$$B = \frac{-4\beta^2 p\eta_\alpha\left(1-2\beta^2p^2\right)}{\left(1-2\beta^2p^2\right)^2 + 4\beta^4p^2\eta_\alpha\eta_\beta + i\frac{\eta_\alpha}{\rho\omega}k}. \tag{25}$$

Eqs (24) and (25) define the reflection coefficients of *PP* and *PS* waves for the unified boundary. Note that the reflection coefficients of *PP* and *PS* waves are complex numbers when $\frac{\eta_\alpha}{\rho\omega}k$ is nonzero, and it can result in additional phase shift, that is, time shift in the reflected waves. For the case of free boundary condition ($k = 0$), the *PP* and *PS* reflection coefficients are same as eqs 5.25 and 5.26 in Aki & Richards (2002), implying that the above derivation is correct.

Combining eqs (24) and (13) or (14), we find that the *PP* reflection coefficient relies on angular frequency ω and H as well as slowness p, unlike the case of free boundary condition where the *PP* reflection coefficient is frequency independent. After Lay & Wallace (1995), we define a dimensionless frequency

$$\Omega = \frac{\omega H}{\alpha_w}. \tag{26}$$

It is straightforward that the reflection coefficient of *PP* waves only relies on the dimensionless frequency Ω and slowness p.

As the amplitude ratio and differential time between *PP* and its precursors are used to determine the velocity contrast and depth of 410 and 660 km mantle discontinuities, we calculate the amplitude and phase of *PP* reflection coefficient with different dimensionless frequency Ω and slowness p, respectively. The range of dimensionless frequency Ω is chosen according to the period of teleseismic *PP* used in previous studies. Usually, the filtering range is between 8 and 75 s (Flanagan & Shearer 1999; Chambers *et al.* 2005; Deuss *et al.* 2006; Deuss 2009) and then the range of dimensionless frequency is $0.22 \leq \Omega \leq 2.09$, assuming an average ocean thickness of 4 km (Stewart 2004). Slowness p can be calculated from epicentral distances from $80^\circ \leq \Delta \leq 140^\circ$ (Flanagan & Shearer 1999; Shearer & Flanagan 1999; Deuss 2009) and then the range of slowness is found to be $0.055\ \text{s km}^{-1} \leq p \leq 0.075\ \text{s km}^{-1}$ with the TAUP program (Crotwell *et al.* 1999) for the PREM model (Dziewonski & Anderson 1981).

In Fig. 3, the absolute amplitude of *PP* reflection coefficient is displayed versus dimensionless frequency Ω and slowness p for the case of a uniform ocean water layer above half-space solid Earth (Table 1). For a given slowness $p = 0.055\ \text{s km}^{-1}$ (Fig. 3a), the amplitude of *PP* reflection coefficient does not change for different dimensionless frequency Ω for the case of free surface boundary ($H = 0$). However, with the WCA boundary condition, the amplitude of *PP* reflection coefficient increases monotonically with dimensionless frequency Ω. In contrast, for the case of exact water column boundary, the amplitude of *PP* reflection coefficient varies periodically with dimensionless frequency Ω, and reaches maximum near the multiplies of $\frac{\pi}{2}$, which is caused by infinity of $\tan(\frac{\pi}{2})$. When Ω is small (<1.0), *PP* amplitude are almost identical for the approximate and the exact water layer condition, suggesting that WCA is valid. Only when Ω is near $\frac{\pi}{2}$, the difference in *PP* amplitude is substantial (up to 13 per cent) between the approximate and exact boundary conditions, in this case the period of *PP* waves is about 11 s for ocean thickness of 4 km. This suggests that 10 s period is too short in using *PP* waves to infer properties of mantle discontinuities, and longer periods are needed. The above features of *PP* amplitude are similar when slowness is different, such as $0.065\ \text{s km}^{-1}$ (Fig. 3b) and $0.075\ \text{s km}^{-1}$ (Fig. 3c).

Then we discuss the variation of *PP* amplitude versus slowness p when dimensionless frequency Ω is fixed (Figs 3d–f for dimensionless frequency Ω of 0.5, 1.0 and 1.5, respectively). For the case of free surface boundary, *PP* amplitude decreases monotonically from 1 to 0 for slowness p in the range of 0–0.16 s km^{-1}, then *PP* amplitude increases for $p > 0.16\ \text{s km}^{-1}$. However, *PP* amplitude increases to 1 rapidly when slowness p is close to $0.2\ \text{s km}^{-1}$. The trend is identical to those described in Lay & Wallace (1995) and Aki & Richards (2002), implying that our numerical implementation is correct. The *PP* amplitudes for the case of approximate and exact water layer boundary is similar to the case of free surface boundary, except that they do not drop to zero at $p = 0.16\ \text{s km}^{-1}$. In the range of slowness p ($0.055\ \text{s km}^{-1} \leq p \leq 0.075\ \text{s km}^{-1}$), *PP* amplitudes are almost same for the approximate and exact water layer boundary when dimensionless frequency $\Omega = 0.5$ or 1.0. But they are quite different when dimensionless frequency $\Omega = 1.5$, which is near $\frac{\pi}{2}$, consistent with Figs 3(a)–(c). Overall, the match in *PP* amplitude between approximate and exact water layer boundary seems to be controlled mostly by dimensionless frequency Ω, and WCA is valid when dimensionless frequency Ω is small (<1.0). In contrast, the validity is much less sensitive to slowness p, though it can be observed that the error of WCA is a little bit larger when p changes from 0.055 to $0.075\ \text{s km}^{-1}$.

Similarly, we investigate variation of the phase of *PP* reflection coefficient versus dimensionless frequency Ω and slowness p. In

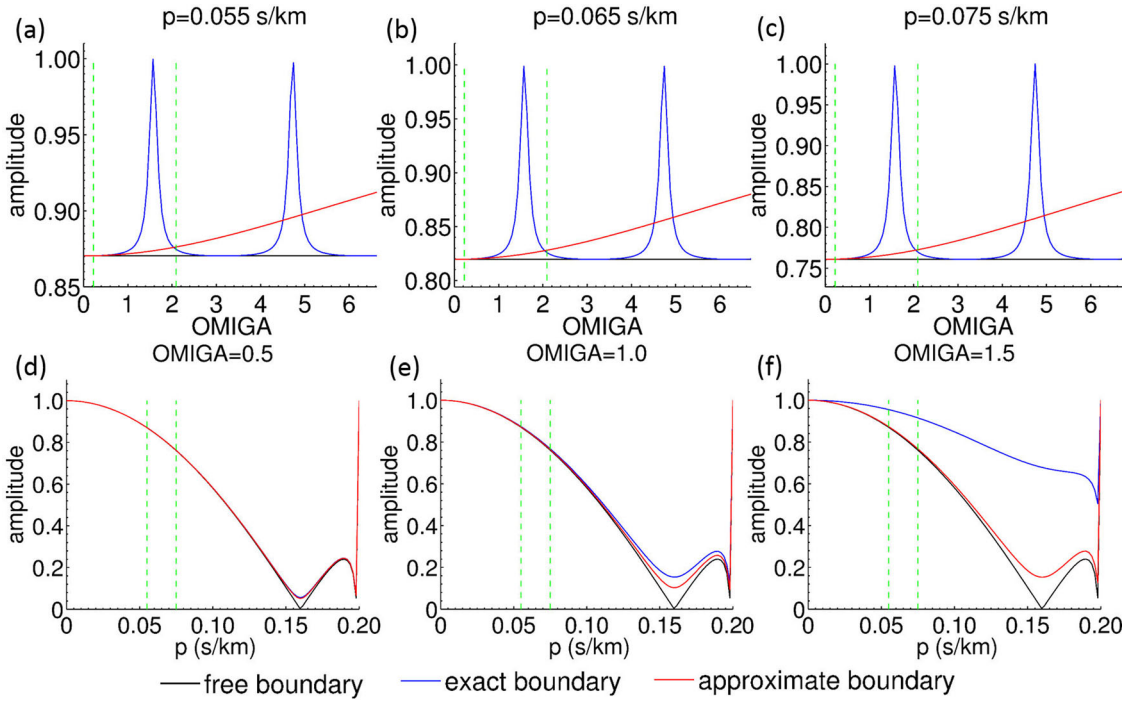

Figure 3. *PP* reflection coefficient amplitude versus dimensionless frequency Ω (a–c), or versus slowness p (d–f). Black, red and blue lines indicate cases of free boundary condition, exact boundary condition and approximate boundary condition. The green dashed lines indicate the range of dimensionless frequency or slowness usually adopted in studies of teleseismic *PP* wave.

Table 1. Parameters of the ocean water layer and the half-space solid Earth.

Depth to bottom (km)	ρ (g cm^{-3})	β (km s^{-1})	α (km s^{-1})
4.0	1.00	0.00	1.50
∞	3.00	3.00	5.00

Fig. 4(a), the slowness p is 0.055 s km^{-1}. For the case of free surface boundary, the *PP* phase is does not change with different dimensionless frequency Ω and is -180° ($-\pi$), consistent with the fact that *PP* reflection coefficient is negative real number (Aki & Richards 2002). However, for the case of approximate water layer boundary, *PP* phase increases monotonically with dimensionless frequency Ω. In contrast, for exact water column boundary, *PP* phase changes periodically with dimensionless frequency Ω, and the largest gradient is near the integer times of $\pi/2$. When Ω is small (<1.0), *PP* phase is almost identical for the approximate and exact water layer boundary, arguing that WCA is valid. But when Ω is near $\pi/2$, the difference in *PP* phase is substantial, similar to the pattern for *PP* amplitude versus Ω. The above pattern of *PP* phase variation is similar for different slowness (Fig. 4b, $p = 0.065$ s km^{-1}; Fig. 4c, $p = 0.075$ s km^{-1}). In Figs 4(d)–(f), variation of *PP* phase versus slowness p is displayed for Ω of 0.5, 1.0 and 1.5, respectively, and we observe that *PP* phase does not change much for the slowness range of teleseismic *PP* waves (0.055–0.075 s km^{-1}). For small Ω (0.5, Fig. 4d), *PP* phase with WCA matches that with exact boundary condition very well. But for $\Omega = 1.0$, there is phase difference about 5°. Actually, Ω of 1.0 corresponds to period of 17 s for ocean water depth H of 4 km and water speed of 1.5 km s^{-1}. Thus 5° phase difference is equivalent to time shift of 17 × 5/360 s–0.2 s, or change of 1 km in estimating depth of mantle discontinuity (assuming average mantle *P* velocity of 10 km s^{-1}). And for $\Omega = 1.5$ (the period of *PP* waves is around 10 s for ocean thickness H of 4 km), the phase difference is up to 90°. In this case, the mismatch in *PP* phase is equivalent to time shift of a quarter of the period of *PP* waves (2.5 s), which may cause error of 12.5 km in estimating depth of mantle discontinuity. Therefore, *PP* waves with period much longer than 10 s should be used to resolve depth of mantle discontinuity, when WCA is adopted in numerical simulations. Therefore, both Figs 3 and 4 argue that validity of WCA is mainly controlled by Ω instead of slowness p. And this is not unexpected, as k in the unified boundary condition is the controlling parameter and it much more depends upon Ω than slowness.

As the water depth in oceanic region varies substantially from dozens of meters to ten thousand meters, it would be helpful to quantify validity of WCA for global ocean. We define critical period as the minimum period of *PP* waves which lead to error in *PP* amplitude less than 5 per cent and phase difference less than 9°. The error of 5 per cent is chosen because usually 10 per cent error is usually adopted as a small number, and an error of 9° in phase is equivalent to 2.5 per cent of period of *PP* waves, which is also usually viewed as very small error. Slowness p of 0.075 s km^{-1} is chosen in the computation. For every 5 × 5 min^2 area of oceanic region, we extract water depth from ETOP5 model (Edwards 1988) and compute the critical period beyond which WCA is valid. From Fig. 5(a), we observe that the critical period for 5 per cent accuracy in *PP* amplitude is 25 s for most area of the oceans, about or less than 5 s in shallow seas, about 15 s near mid-ocean ridges and about 40 s at deep trenches. From Fig. 5(b), we observe that the critical period for 9° accuracy in *PP* phase is about 30 s for most area of global oceans, about or less than 5 s in the shallow seas, about 20 s near mid-ocean ridges and around 45 s at deep trenches.

We also generate a map of error in *PP* amplitude (Supporting Information Fig. S1) and time shift due to *PP* phase error (Supporting Information Fig. S2) at various periods. At period of 15 s,

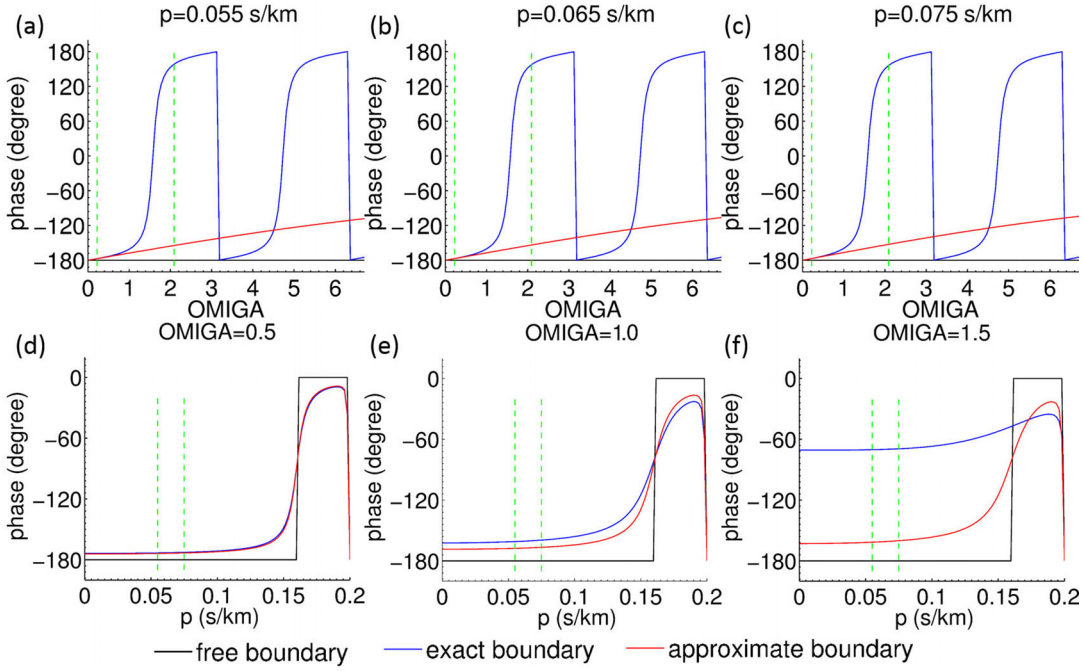

Figure 4. *PP* phase shift versus dimensionless frequency Ω (a–c), or versus slowness p (d–f). Black, red and blue lines indicate cases of free boundary condition, exact boundary condition and approximate boundary condition. The green dashed lines indicate the range of dimensionless frequency or slowness usually adopted in studies of teleseismic *PP* wave.

the error in *PP* amplitude is larger than 10 per cent in most part of the Pacific Ocean, deep ocean basin of Atlantic Ocean and near mid-ocean ridges. At period of 20 s, the error is less than 2 per cent for majority of oceanic regions. At period of 25 s, the error is less than 1 per cent in most part of global oceans, except near very deep trenches. Supporting Information Fig. S2 shows distribution of time shift due to WCA, which is obtained by multiplying period of *PP* waves and the phase shift relative to 2π. At period of 15 s, the time shift is more than 5 s in some area of the Pacific Ocean, deep basin of Atlantic Ocean and near mid-ocean ridges. At period of 20 s, the time shift is less than 1 s. And at period of 25 s, the time shift is very small for most part of the ocean, except near deep trenches. Both Supporting Information Figs S1 and S2 suggest that WCA is valid at period of 25 s or longer.

4 THE EFFECTS ON SURFACE WAVE OF WCA

Calculation of Rayleigh wave dispersion is a classical problem in seismology, and many methods have been developed. For a flat-layered Earth model, Thomson & Haskell (Thomson 1950; Haskell 1953) proposed the propagation matrix method (also called as Thomson-Haskell method) to solve the eigenvalue problem of the system of differential equations. But this method is sometimes unstable and suffers numerical overflow and loss of precision at high frequency (Buchen & Ben-Hador 1996; Wang 1999; Kennett 2009). Later on, many improvements on Thomson-Haskell method are adopted to overcome these problems, such as the delta matrix method (Pestel & Leckie 1963; Watson 1970; Wang & Herrmann 1980; Buchen & Ben-Hador 1996), Schwab–Knopoff method (Schwab 1970; Schwab & Knopoff 1970, 1972), Abo-Zena method (Abo-Zena 1979), Kennett reflection and transmission (R/T) matrix method (Kennett 1974; Kennett & Kerry 1979) and generalized R/T coefficient method (Luco & Apsel 1983; Chen 1993; Pei *et al.* 2008, 2009; Kennett 2009). Even though R/T methods are not necessarily the most efficient one of these improved methods (Buchen & Ben-Hador 1996), they are more numerically stable at high frequency. For example, Chen's method is one of the generalized R/T coefficient methods, and can calculate phase velocity at frequency higher than 100 Hz (Chen 1993). Moreover, free surface boundary condition is explicitly imposed in Chen's algorithm, which can be straightforwardly extended for new boundary condition. Therefore, we adopt Chen's method to compute Rayleigh wave dispersion for the case of unified boundary condition and quantify the accuracy of WCA in simulating Rayleigh wave propagation. Of course classical normal modes code or other propagation matrix code can also be extended for new boundary condition, and this will be done in the future.

As the published generalized R/T method only implemented free surface boundary condition, we will reformulate the method so as to account for the unified boundary condition. For the model of a fluid layer above layered solid Earth and convention of coordinate system shown in Fig. 6, the wavefield of *P–SV* wave in jth layer can be described with the displacement vector $D^{(j)} = [\, U_r \;\; U_z \,]^T$ and stress vector $\Sigma^{(j)} = [\, \Sigma_{rz} \;\; \Sigma_{zz} \,]^T$ which can be solved with the following ordinary differential equations in depth z:

$$\frac{\mathrm{d}}{\mathrm{d}z}\begin{pmatrix} D^{(j)}(z) \\ \Sigma^{(j)}(z) \end{pmatrix} = A^{(j)}\begin{pmatrix} D^{(j)}(z) \\ \Sigma^{(j)}(z) \end{pmatrix}. \tag{27}$$

For each homogeneous layer, the displacement and stress vector can be computed with amplitudes of upgoing and downgoing waves (C_u and C_d):

$$\begin{pmatrix} D^{(j)}(z) \\ \Sigma^{(j)}(z) \end{pmatrix} = \begin{pmatrix} {E^{(j)}}_{11} & {E^{(j)}}_{12} \\ {E^{(j)}}_{21} & {E^{(j)}}_{22} \end{pmatrix}\begin{pmatrix} \Lambda_d^{(j)}(z) & 0 \\ 0 & \Lambda_u^{(j)}(z) \end{pmatrix}\begin{pmatrix} C_d^{(j)} \\ C_u^{(j)} \end{pmatrix} \tag{28}$$

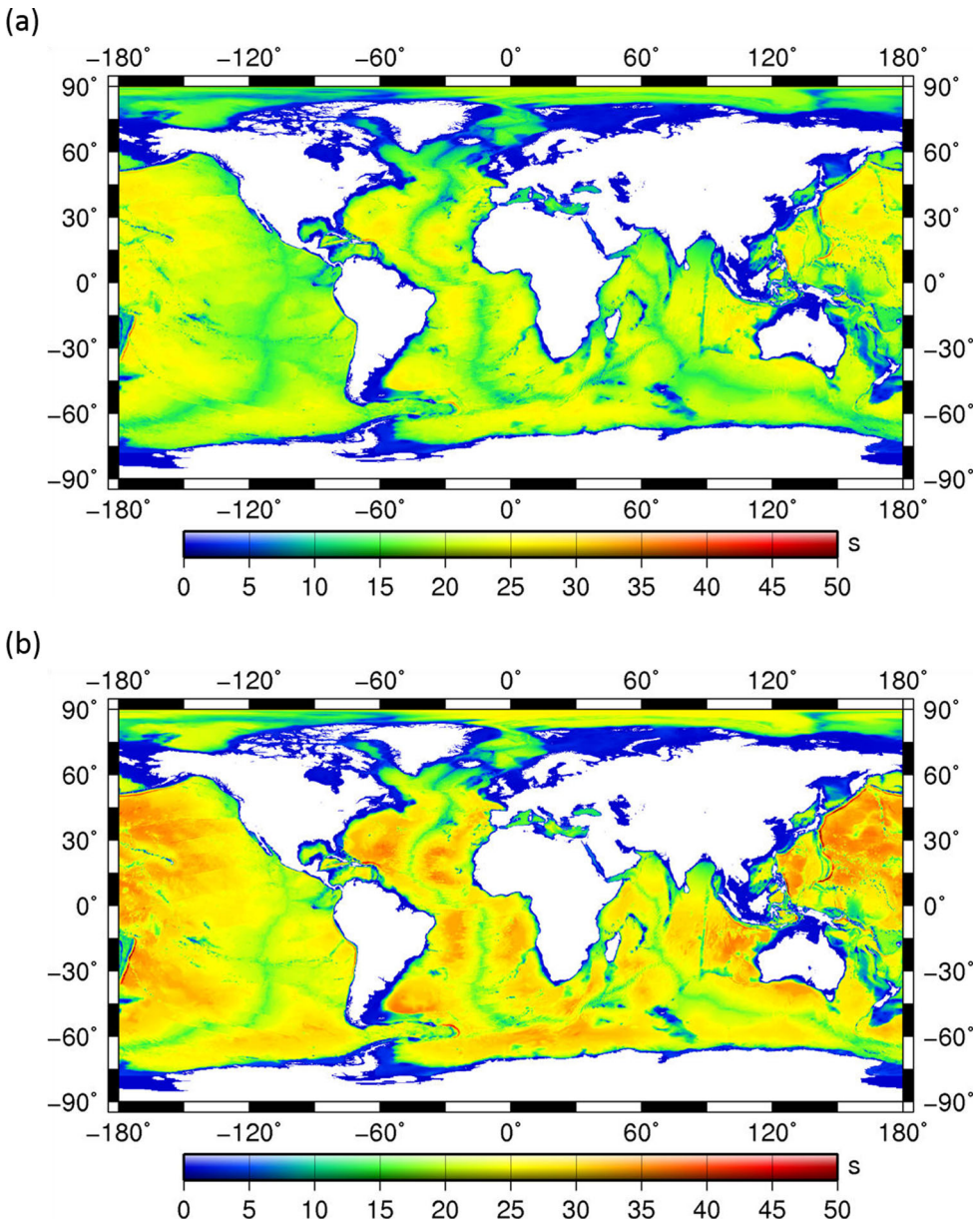

Figure 5. The critical periods for *PP* wave with WCA: (a) for amplitude error ≤5 per cent; (b) for phase shift ≤9°.

where E and Λ are defined in Chen (1993). Then the generalized reflection and transmission coefficients ($\hat{R}_{du}$ and $\hat{T}_d$) are defined accordingly:

$$\begin{cases} C_u^{(j)} = \hat{R}_{du}^{(j)} C_d^{(j)} \\ C_d^{(j+1)} = \hat{T}_d^{(j)} C_d^{(j)} \end{cases}. \tag{29}$$

And in his formulation, the free surface boundary condition is reduced to the following equation:

$$1 - \hat{R}_{ud}^{(0)} \hat{R}_{du}^{(1)} = 0 \tag{30}$$

and

$$\hat{R}_{ud}^{(0)} = -\left(E_{21}^{(1)}\right)^{-1} E_{22}^{(1)} \Lambda_u^{(1)}(0). \tag{31}$$

In our method, the free boundary can be readily adapted for the unified boundary condition

$$\hat{R}_{ud}^{(0)} = -\left(E_{21}^{(1)} - K E_{11}^{(1)}\right)^{-1} \left(E_{22}^{(1)} - K E_{12}^{(1)}\right) \Lambda_u^{(1)}(0), \tag{32}$$

where K is a 2×2 sparse matrix involving of k, the coefficient defined in eq. (12):

$$K = \begin{bmatrix} 0 & 0 \\ 0 & k \end{bmatrix}. \tag{33}$$

When $k = 0$, eq. (32) is reduced to the eq. (31). After imposing eq. (32), Chen's (1993) method is readily modified to calculate the Rayleigh wave phase velocity for the case of a fluid layer above solid media with WCA or exact boundary conditions.

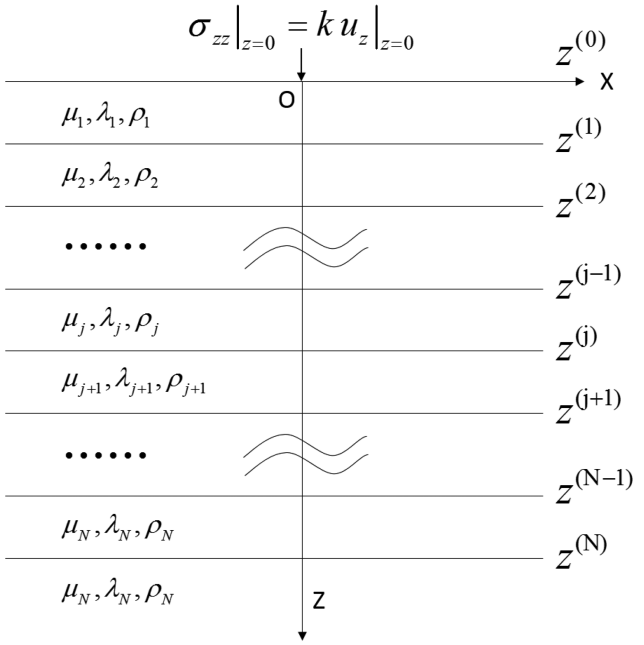

Figure 6. Configuration and coordinate system of a multilayered half-space with the unified boundary condition.

However, the matrix method still fails at high frequency. In this case, Rayleigh wave energy is only concentrated in the top solid layer, which is essentially equivalent to half-space. It is difficult to compute the fundamental mode phase velocity of Rayleigh wave from the secular function in this situation (Chen 1993). To solve this problem, Chen (1993) developed an asymptotic method that involves the boundary condition. Therefore, the asymptotic method needs to be reformulated to account for the unified boundary with water layers. After plugging eqs (12) and (29) into eq. (28), we obtain

$$\left[\left(E_{21}^{(1)} - KE_{11}^{(1)}\right) + \left(E_{22}^{(1)} - KE_{12}^{(1)}\right)\Lambda_u(0)\,\hat{R}_{du}^{(1)}\right] C_d^{(1)} = 0. \quad (34)$$

Eq. (34) has a non-trivial solution only for some particular phase velocities that satisfy the following secular equation

$$\det\left[\left(E_{21}^{(1)} - KE_{11}^{(1)}\right) + \left(E_{22}^{(1)} - KE_{12}^{(1)}\right)\Lambda_u(0)\,\hat{R}_{du}^{(1)}\right] = 0. \quad (35)$$

Following Chen (1993), we define $E_{21}^{(1)} - KE_{11}^{(1)} = \omega A(c)$ and $(E_{22}^{(1)} - KE_{12}^{(1)})\Lambda_u(0)\hat{R}_{du}^{(1)} = \omega B(c)$, then use his eqs (A7)–(A9) to calculate the Rayleigh wave phase velocity at high frequency, via introducing eq. (36) which is derived from eq. (27) and eq. (9) of Chen (1993). Chen's (1993) method also involves of a parameter cR which is the value of c when function $R(c)$ (in eq. 36) equals to 0.

$$R(c) = 4\left(\frac{1}{c}\right)^2 \bar{\gamma}^{(1)}(c)\bar{\nu}^{(1)}(c) - \left\{\left(\frac{1}{c}\right)^2 + (\bar{\nu}^{(1)}(c))^2\right\}^2 - \frac{i\eta_\alpha}{\rho\beta^4\omega}k. \quad (36)$$

With the algorithm for both low frequency and high frequency illustrated, we implement a computer code (RTgen) for computing fundamental mode Rayleigh wave phase velocity dispersion with MATLAB language. To test the code, we choose the case of 4 km thick water layer above the layered solid crustal model (Table 2). To verify that our implemented code works correctly, we also use the CPS package (Wang & Herrmann 1980; Herrmann 2013) to compute fundamental Rayleigh phase velocity for free surface boundary

Table 2. Parameters of the ocean water layer above layered crustal model.

H (km)	ρ (g cm^{-3})	β (km s^{-1})	α (km s^{-1})
h	1.00	0.00	1.50
3.0	2.61	2.59	5.09
3.0	2.90	3.65	6.60
3.0	3.05	3.91	7.11
∞	3.35	4.65	8.15

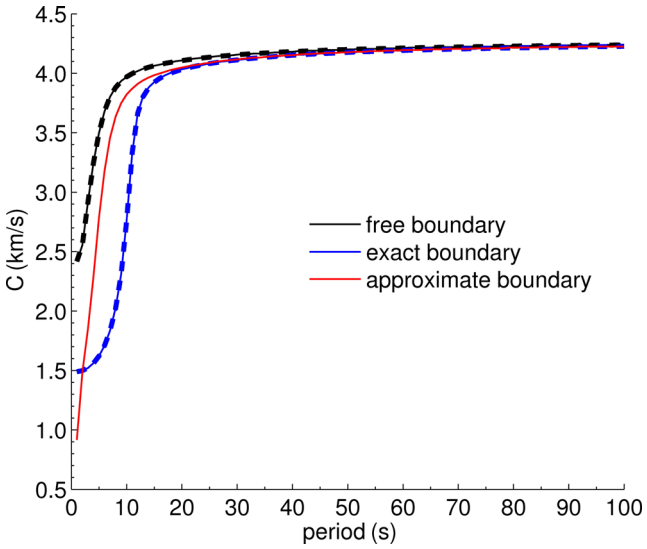

Figure 7. Comparison of fundamental phase velocity computed by RTgen (solid line) and CPS (dash line) with the velocity model in Table 2, for the cases of free boundary condition (black), exact boundary condition (blue) and approximate boundary condition (red). The water layer thickness is 4 km.

condition and water layer in which exact boundary conditions are satisfied at the interface between water and crust. In Fig. 7, a comparison between phase velocity from RTgen and CPS is displayed, showing excellent matches for the free surface case (solid line for RTgen and dash line for CPS), as well as for the case of accurate water column boundary, implying correct implementation of algorithms in RTgen. As for the comparison of fundamental mode phase velocity with approximate and exact water column boundary, the former is very close to the latter in long periods ($T > 20$ s), which indicates that the validity of WCA to represent the effects of oceanic layer on Rayleigh waves. But at shorter periods ($2\text{ s} < T < 20$ s), the fundamental mode phase velocity with WCA is larger than the one with exact water column boundary. At even shorter periods ($T < 2$ s), the phase velocity with WCA drops sharply and differs from that with exact boundary condition, suggesting that the WCA is no longer effective to account for the effects of water layer on Rayleigh waves at high frequency.

The accuracy of WCA for different ocean depths ($H = 0.2$, 1.0, 4.0 and 8.0 km) is displayed in Fig. 8. For the ocean depth H of 0.2 km, the phase velocities for free surface, approximate boundary and exact boundary condition are almost the same for periods above 2 s. This is understandable because the 0.2 km thickness is much shorter than the wavelength, and the ocean is just thin enough to be negligible. For the ocean depth H of 1.0 km, the phase velocity with approximate and exact boundary condition matches with each other at periods over 15 s. But for periods less than 5 s, their mismatch is substantial, suggesting that approximate boundary condition no longer works. The case of 4.0 km ocean depth has been described in

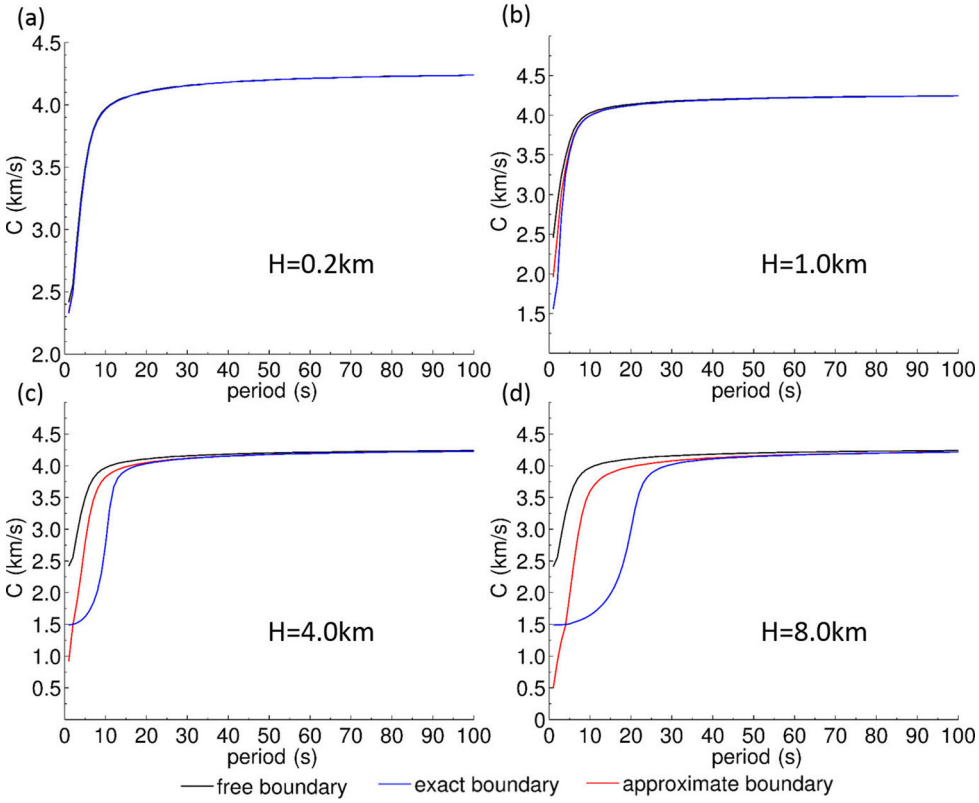

Figure 8. Comparison of fundamental phase velocity dispersion with different water layer depth, for the cases of free boundary condition (black), exact boundary condition (blue) and approximate boundary condition (red).

Fig. 7. And for the ocean depth of 8.0 km, the comparison between approximate and exact boundary condition is similar to the case of 4.0 km depth, except that their phase velocities are very close only at periods longer than 30 s.

To quantify the accuracy of WCA for global ocean, we generate the map of critical period beyond which the mismatch of phase velocity between approximate and exact boundary condition is less than 5 per cent. We extract the ocean water depth and crustal models from the CRUST 2.0 model (Bassin *et al.* 2000) in $2^\circ \times 2^\circ$ grids. As shown in Fig. 9, in most part of ocean regions, the critical period is 15 s. But for a substantial part of the northwestern Pacific Ocean and some parts of the Atlantic Ocean, the critical period is about 20 s, as the result of deeper ocean. Near mid-ocean ridges where ocean is a little bit shallower, the critical period is about 10 s, and for shallow sea, the critical period is less than 5 s. The effects due to deep trenches are not observed on this figure, probably because bathymetric features of narrow trenches are smoothed out with $2^\circ \times 2^\circ$ sampling.

We also quantify the accuracy of WCA in computing Rayleigh wave phase velocity for the global ocean at given periods (Supporting Information Fig. S3). At period of 20 s, the error is larger than 2 per cent in substantial part of deep oceans, and is less than 1 per cent near mid-ocean ridges or shallow sea regions. At period of 25 s, the error is less than 1 per cent for majority part of oceans. At periods of 30 s, the discrepancy is less than 1 per cent in almost all the oceanic region. This suggests that WCA at periods longer than 25 s is sufficient to account for effects of water layer, leading to error less than 1 per cent which is smaller than 2–3 per cent lateral variation in various tomography models (Ekström 2011).

5 DISCUSSION

From above analysis, we find that the WCA is accurate in simulating both *PP* and Rayleigh waves at periods longer than 25 s for most part of global oceans. This result is consistent with the qualitative conclusion by Komatitsch & Tromp (2002b), who find that WCA becomes invalid at periods shorter than typically 20 s (Komatitsch *et al.* 2005; Chaljub *et al.* 2007). If the error bound is relaxed (e.g. *PP* amplitude error < 10 per cent or Rayleigh wave dispersion error < 2 per cent), WCA can indeed be used for periods as low as 20 s (Supporting Information Figs S1 and S3). But at even shorter periods (down to 10 s), the *PP* amplitude is substantially lower than the value from the exact boundary condition (Figs 3a–c, for average ocean depth of 4 km). Ritsema *et al.* (2002) used SEM with WCA to investigate the global amplitude ratio of *PP*/*P* at periods longer than 16 s and found that *PP*/*P* amplitude ratio is about 10 per cent lower than PREM. Although they proposed that 3-D heterogeneity could be the reason, we suggest that lower amplitude due to WCA could also partly contribute to the smaller *PP*/*P* ratio. For example, as demonstrated in Supporting Information Fig. S1(a), *PP* amplitude with WCA is 10 per cent lower at period of 15 s for deep basin of Pacific and Atlantic oceans. In observational studies of *PP* precursors, period down to 8 s has been used (Deuss *et al.* 2006). Therefore, caution needs to be taken if SEM or other numerical solvers are used to simulate global *PP* waves at this frequency band.

However, we have only analysed very idealized situation with uniform ocean layer above flat horizontal seafloor, and have not studied the effects of seafloor topography and stratification of ocean water due to layering of temperature and salinity. For the case of a flat

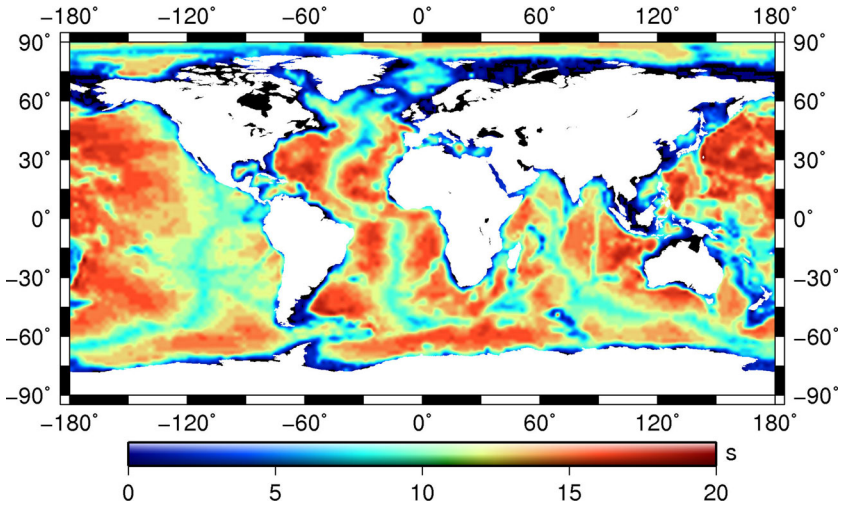

Figure 9. Global distribution of critical periods for Rayleigh wave dispersion error less than 5 per cent.

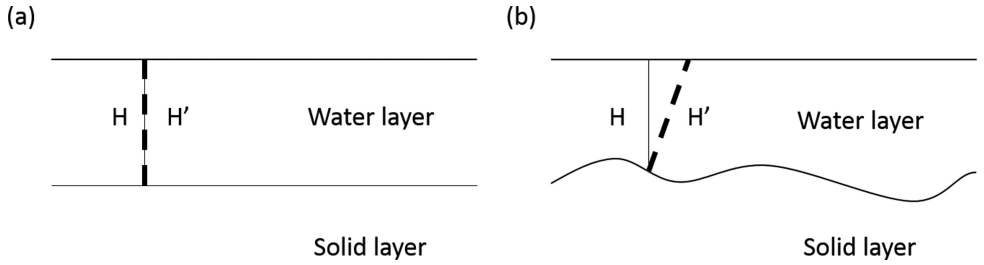

Figure 10. Schematic drawing of flat (a) and undulating (b) seafloor. For the case of flat seafloor, the thickness H along vertical direction (plumb line) and the thickness H' along the normal direction are same. But they differ for the case of undulating seafloor.

horizontal floor, the vertical direction is same as the normal direction to the seafloor, but these two directions are different for the case of undulating seafloor. Therefore, the vertical depth of ocean water (H) is usually different from the depth in the normal direction (H') (Fig. 10). Furthermore, the slope of seafloor may have some effect on the *PP* reflection coefficients. However, the slope of seafloor is usually very small, except regions near volcanoes in the ocean (Stewart 2004). Probably, the slope of realistic seafloor only has second order effects, and does not substantially affect WCA, which is a first order approximation. Moreover, stratification of ocean water is also minor compared to layering in the solid Earth, and will probably not obviously bias our results in this paper. The influences of these second-order effects can be verified on a regional scale using the SEM code implemented with the approximate or exact boundary condition across seafloor (Komatitsch *et al.* 2000).

However, we only analysed accuracy of WCA in simulating *PP* reflection coefficient and Rayleigh wave phase velocity at individual periods. But in the practical studies of observed *PP* waves, the seismic waveform data are usually modelled in a frequency band instead of at one frequency, for example, 8–75 s and 15–75 s in Deuss (2009). Therefore, more detailed assessment of accuracy of the *PP* amplitude should be conducted via integration over the frequency band. Furthermore, *PP* waves are not reflected at a point, but within a broad Fresnel zone, and Rayleigh waves also propagate in a finite volume instead of along an infinitely thin ray. Theoretically, more quantitative study of the accuracy of WCA should also be performed via integration over the whole Fresnel zone. With those being said, the analysis in this paper provides a basic quantification of the accuracy of WCA.

6 CONCLUSIONS

Usually WCA is used in SEM and other numerical solvers to account for effects of global ocean structure, so as to reduce cost of computation time and memory in global seismic wave simulation because the ocean layer is not meshed explicitly. However, it is only valid when the ocean is shallow as compared to seismic wave length. In this paper, we quantify the accuracy of WCA in simulating *PP* and Rayleigh waves at different depths of ocean from hundreds of meters to 10 km. Based on plane wave theory, we derive a unified boundary condition for a homogeneous water layer above the solid Earth. We analyse its accuracy in simulating *PP* reflection and Rayleigh wave dispersion for different ocean depths and periods, via deriving an analytical form of *PP*-wave reflection coefficient and implementing a matrix-based method in calculating eigenfunction of fundamental mode Rayleigh wave. We find that WCA is sufficiently accurate for global ocean at periods longer than 25 s, and is valid for most part of the global ocean at periods longer than 20 s. But at periods of 15 s or lower, the approximation may lead to 10 per cent or larger error in *PP* amplitude and a few seconds time shift in *PP* arrival, as well as up to 2 per cent error in Rayleigh wave dispersion, for substantial part of deep oceans. Therefore, it is safe to use SEM and other numerical solvers with WCA in simulating global seismic waves at periods of 25 s and longer, but caution should be taken when simulating seismic waves at shorter periods.

As the current version of WCA only takes advantage of the first term in Taylor expansion of the exact boundary condition, it could be improved via higher order terms. But, it is technically difficult to implement in SEM with order 2 and higher of the exact

boundary condition as it implies the gradient value of the wavefield. An effective algorithm has been proposed by Capdeville & Marigo (2008) to account for complexity near free surface with accuracy up to order 2. Alternatively, it could also be improved via imposing the exact boundary condition, which involves of a nonlinear function of the vertical slowness. In this case, horizontal and vertical slowness needs to be estimated by analysing local plane wavefield generated in SEM simulations, thus requiring extra coding efforts. Another way is to calibrate the effects of the water layer on *PP* reflection and Rayleigh dispersion assuming given slowness in a 1-D Earth model, but its effectiveness needs to be benchmarked in the future.

ACKNOWLEDGEMENTS

We are grateful that Yann Capdeville and an anonymous reviewer provided constructive suggestions, and Professor R. Herrmann kindly shared the CPS code. We also thank Dr Carl Tape for his helpful comments. This study is supported by China 973 Basic Research Program 2014CB845901 and NSFC 41274069.

REFERENCES

Abo-Zena, A., 1979. Dispersion function computations for unlimited frequency values, *Geophys. J. Int.,* **58,** 91–105.

Aki, K. & Richards, P.G., 2002. *Quantitative Seismology,* University Science Books.

Baker, B. & Roecker, S., 2014. A full waveform tomography algorithm for teleseismic body and surface waves in 2.5 dimensions, *Geophys. J. Int.,* **198,** 1775–1794.

Bao, H., Bielak, J., Ghattas, O., Kallivokas, L.F., O'Hallaron, D.R., Shewchuk, J.R. & Xu, J., 1998. Large-scale simulation of elastic wave propagation in heterogeneous media on parallel computers, *Comput. Meth. Appl. Mech. Eng.,* **152,** 85–102.

Bassin, C.G.L., Laske, G. & Masters, G., 2000. The current limits of resolution for surface wave tomography in North America, *EOS, Trans. Am. geophys. Un.,* **81**(48), Fall Meet. Suppl., Abstract S12A-03.

Bozdağ, E. & Trampert, J., 2008. On crustal corrections in surface wave tomography, *Geophys. J. Int.,* **172,** 1066–1082.

Buchen, P. & Ben-Hador, R., 1996. Free-mode surface-wave computations, *Geophys. J. Int.,* **124,** 869–887.

Capdeville, Y. & Marigo, J.-J., 2008. Shallow layer correction for spectral element like methods, *Geophys. J. Int.,* **172,** 1135–1150.

Capdeville, Y., Gung, Y. & Romanowicz, B., 2005. Towards global earth tomography using the spectral element method: a technique based on source stacking, *Geophys. J. Int.,* **162,** 541–554.

Chaljub, E., Komatitsch, D., Vilotte, J.-P., Capdeville, Y., Valette, B. & Festa, G., 2007. Spectral-element analysis in seismology, *Adv. Geophys.,* **48,** 365–419.

Chambers, K., Deuss, A. & Woodhouse, J., 2005. Reflectivity of the 410-km discontinuity from PP and SS precursors, *J. geophys. Res.,* **110,** doi:10.1029/2004JB003345.

Chen, M., Niu, F., Liu, Q. & Tromp, J., 2015. Mantle-driven uplift of Hangai Dome: new seismic constraints from adjoint tomography, *Geophys. Res. Lett.,* **42,** 6967–6974.

Chen, X., 1993. A systematic and efficient method of computing normal modes for multilayered half-space, *Geophys. J. Int.,* **115,** 391–409.

Cormier, V.F., 2000. D″ as a transition in the heterogeneity spectrum of the lowermost mantle, *J. geophys. Res,* **105,** 16 193–16 205.

Crotwell, H.P., Owens, T.J. & Ritsema, J., 1999. The TauP Toolkit: Flexible seismic travel-time and ray-path utilities, *Seismol. Res. Lett.,* **70,** 154–160.

Deuss, A., 2009. Global observations of mantle discontinuities using SS and PP precursors, *Surv. Geophys.,* **30,** 301–326.

Deuss, A., Redfern, S.A., Chambers, K. & Woodhouse, J.H., 2006. The nature of the 660-kilometer discontinuity in Earth's mantle from global seismic observations of PP precursors, *Science,* **311,** 198–201.

Dziewonski, A.M. & Anderson, D.L., 1981. Preliminary reference Earth model, *Phys. Earth planet. Inter.,* **25,** 297–356.

Edwards, M., 1988. *Data Announcement 88-MGG-02: Digital Relief of the Surface of the Earth,* National Oceanic and Atmospheric Administration, National Geophysical Data Center.

Ekström, G., 2011. A global model of Love and Rayleigh surface wave dispersion and anisotropy, 25–250 s, *Geophys. J. Int.,* **187,** 1668–1686.

Flanagan, M.P. & Shearer, P.M., 1999. A map of topography on the 410-km discontinuity from PP precursors, *Geophys. Res. Lett.,* **26,** 549–552.

French, S.W. & Romanowicz, B., 2015. Broad plumes rooted at the base of the Earth's mantle beneath major hotspots, *Nature,* **525,** 95–99.

Fukao, Y., To, A. & Obayashi, M., 2003. Whole mantle *P* wave tomography using P and PP-P data, *J. geophys. Res.,* **108,** ESE 8-1–ESE 8–14.

Haskell, N.A., 1953. The dispersion of surface waves on multilayered media, *Bull. seism. Soc. Am.,* **43,** 17–34.

Herrmann, R.B., 2013. Computer programs in seismology: an evolving tool for instruction and research, *Seismol. Res. Lett.,* **84,** 1081–1088.

Igel, H., Mora, P. & Riollet, B., 1995. Anisotropic wave propagation through finite-difference grids, *Geophysics,* **60,** 1203–1216.

Kennett, B., 1974. Reflections, rays, and reverberations, *Bull. seism. Soc. Am.,* **64,** 1685–1696.

Kennett, B., 2009. *Seismic Wave Propagation in Stratified Media,* ANU Press.

Kennett, B. & Kerry, N., 1979. Seismic waves in a stratified half space, *Geophys. J. Int.,* **57,** 557–583.

Komatitsch, D. & Tromp, J., 2002a. Spectral-element simulations of global seismic wave propagation—I. Validation, *Geophys. J. Int.,* **149,** 390–412.

Komatitsch, D. & Tromp, J., 2002b. Spectral-element simulations of global seismic wave propagation—II. Three-dimensional models, oceans, rotation and self-gravitation, *Geophys. J. Int.,* **150,** 303–318.

Komatitsch, D., Barnes, C. & Tromp, J., 2000. Wave propagation near a fluid-solid interface: a spectral-element approach, *Geophysics,* **65,** 623–631.

Komatitsch, D., Ritsema, J. & Tromp, J., 2002. The spectral-element method, Beowulf computing, and global seismology, *Science,* **298,** 1737–1742.

Komatitsch, D., Tsuboi, S. & Tromp, J., 2005. The spectral-element method in seismology, in *Seismic Earth: Array Analysis of Broadband Seismograms,* Geophysical Monograph Series 157, eds Levander, A. & Nolet, G., American Geophysical Union, 205.

Lay, T. & Wallace, T.C., 1995. *Modern Global Seismology,* Academic Press.

Liu, K. & Zhou, Y., 2013. Effects of crustal thickness variations on surface wave phase delays, *Geophys. J. Int.,* **192,** 773–792.

Liu, Q., Polet, J., Komatitsch, D. & Tromp, J., 2004. Spectral-element moment tensor inversions for earthquakes in southern California, *Bull. seism. Soc. Am.,* **94,** 1748–1761.

Luco, J.E. & Apsel, R.J., 1983. On the Green's functions for a layered half-space. Part I, *Bull. seism. Soc. Am.,* **73,** 909–929.

Moczo, P., Kristek, J., Galis, M., Pazak, P. & Balazovjech, M., 2007. The finite-difference and finite-element modeling of seismic wave propagation and earthquake motion, *Acta Phys. Slovaca,* **57,** 177–406.

Niklasson, A.J., Datta, S.K. & Dunn, M.L., 2000. On approximating guided waves in plates with thin anisotropic coatings by means of effective boundary conditions, *J. acoust. Soc. Am.,* **108,** 924–933.

Pei, D., Louie, J.N. & Pullammanappallil, S.K., 2008. Improvements on computation of phase velocities of Rayleigh waves based on the generalized R/T coefficient method, *Bull. seism. Soc. Am.,* **98,** 280–287.

Pei, D., Louie, J.N. & Pullammanappallil, S.K., 2009. Erratum to improvements on computation of phase velocities of Rayleigh waves based on the generalized R/T coefficient method, *Bull. seism. Soc. Am.,* **99,** 2610–2611.

Péron, V., 2014. Equivalent boundary conditions for an elasto-acoustic problem set in a Domain with a thin layer, *ESAIM: Math. Modelling Numer. Anal.,* **48,** 1431–1449.

Pestel, E.C. & Leckie, F.A., 1963. *Matrix Methods in Elastomechanics,* McGraw-Hill.

Ritsema, J., Rivera, L.A., Komatitsch, D., Tromp, J. & van Heijst, H.J., 2002. Effects of crust and mantle heterogeneity on PP/P and SS/S amplitude ratios, *Geophys. Res. Lett.,* **29,** 72-71–72-74.

Ruan, Y. & Zhou, Y., 2012. The effects of 3-D anelasticity (Q) structure on surface wave amplitudes, *Geophys. J. Int.,* **189,** 967–983.
Schwab, F., 1970. Surface-wave dispersion computations: Knopoff's method, *Bull. seism. Soc. Am.,* **60,** 1491–1520.
Schwab, F. & Knopoff, L., 1970. Surface-wave dispersion computations, *Bull. seism. Soc. Am.,* **60,** 321–344.
Schwab, F. & Knopoff, L., 1972. Fast surface wave and free mode computations, *Methods Comput. Phys.,* **11,** 87–180.
Shearer, P.M. & Flanagan, M.P., 1999. Seismic velocity and density jumps across the 410- and 660-kilometer discontinuities, *Science,* **285,** 1545–1548.
Stewart, R.H., 2004. *Introduction to Physical Oceanography,* Texas A & M University.
Stich, D. & Morelli, A., 2007. Reflection of seismic surface waves at the northern Apennines, *Earth planet. Sci. Lett.,* **259,** 149–158.
Tape, C., Liu, Q., Maggi, A. & Tromp, J., 2009. Adjoint tomography of the southern California crust, *Science,* **325,** 988–992.
Thomson, W.T., 1950. Transmission of elastic waves through a stratified solid medium, *J. Appl. Phys.,* **21,** 89–93.
Wang, C. & Herrmann, R., 1980. A numerical study of P-, SV-, and SH-wave generation in a plane layered medium, *Bull. seism. Soc. Am.,* **70,** 1015–1036.
Wang, R., 1999. A simple orthonormalization method for stable and efficient computation of Green's functions, *Bull. seism. Soc. Am.,* **89,** 733–741.
Wang, Y., Takenaka, H. & Furumura, T., 2001. Modelling seismic wave propagation in a two dimensional cylindrical whole earth model using the pseudospectral method, *Geophys. J. Int.,* **145,** 689–708.
Watson, T., 1970. A note on fast computation of Rayleigh wave dispersion in the multilayered elastic half-space, *Bull. seism. Soc. Am.,* **60,** 161–166.
Yang, Y., Ritzwoller, M.H., Levshin, A.L. & Shapiro, N.M., 2007. Ambient noise Rayleigh wave tomography across Europe, *Geophys. J. Int.,* **168,** 259–274.
Yao, H., van Der Hilst, R.D. & Maarten, V., 2006. Surface-wave array tomography in SE Tibet from ambient seismic noise and two-station analysis—I. Phase velocity maps, *Geophys. J. Int.,* **166,** 732–744.
Yao, H., Beghein, C. & Van Der Hilst, R.D., 2008. Surface wave array tomography in SE Tibet from ambient seismic noise and two-station analysis-II. Crustal and upper-mantle structure, *Geophys. J. Int.,* **173,** 205–219.
Zakharov, D.D., 2006. High order approximate low frequency theory of elastic anisotropic lining and coating, *J. acoust. Soc. Am.,* **119,** 1961–1970.
Zhang, W. & Chen, X., 2006. Traction image method for irregular free surface boundaries in finite difference seismic wave simulation, *Geophys. J. Int.,* **167,** 337–353.

SUPPORTING INFORMATION

Additional Supporting Information may be found in the online version of this paper:

Figure S1. Error of *PP* amplitude with WCA at period of 15 s (a), 20 s (b) and 25 s (c).
Figure S2. Time shift of *PP* wave with WCA at period of 15 s (a), 20 s (b) and 25 s (c).
Figure S3. Error of Rayleigh wave phase velocity with WCA at period of 20 s (a), 25 s (b) and 30 s (c).
(http://gji.oxfordjournals.org/lookup/suppl/doi:10.1093/gji/ggw212/-/DC1).

Please note: Oxford University Press is not responsible for the content or functionality of any supporting materials supplied by the authors. Any queries (other than missing material) should be directed to the corresponding author for the paper.